OPEN ACCESS

Japanese Journal of Applied Physics **57**, 042501 (2018)

https://doi.org/10.7567/JJAP.57.042501

REGULAR PAPER

Photon-counting-based diffraction phase microscopy combined with single-pixel imaging

Kyuki Shibuya*, Hiroyuki Araki, and Tetsuo Iwata

Graduate School of Tokushima University, Tokushima 770-8506, Japan

*E-mail: shibuya@femto.me.tokushima-u.ac.jp

Received October 4, 2017; accepted January 31, 2018; published online March 20, 2018

We propose a photon-counting (PC)-based quantitative-phase imaging (QPI) method for use in diffraction phase microscopy (DPM) that is combined with a single-pixel imaging (SPI) scheme (PC-SPI-DPM). This combination of DPM with the SPI scheme overcomes a low optical throughput problem that has occasionally prevented us from obtaining quantitative-phase images in DPM through use of a high-sensitivity single-channel photodetector such as a photomultiplier tube (PMT). The introduction of a PMT allowed us to perform PC with ease and thus solved a dynamic range problem that was inherent to SPI. As a proof-of-principle experiment, we performed a comparison study of analogue-based SPI-DPM and PC-SPI-DPM for a 125-nm-thick indium tin oxide (ITO) layer coated on a silica glass substrate. We discuss the basic performance of the method and potential future modifications of the proposed system.

1. Introduction

Quantitative phase (QP) imaging (QPI) is one of the most important techniques available for visualization of the microscale regions of transparent objects and should be developed intensively for applications in fields including biology and semiconductor technology. In particular, QPI's label-free imaging capability allows us to inspect biological cells without use of staining. For this purpose, phase difference-type[1] and differential interference contrast microscopes[2] were developed by Zernike and Smith, respectively. While these microscopes have been used extensively and have become indispensable, the desired QP image cannot be always obtained. This is because these microscopes can only provide an image that has been converted from a "weak-phase-object" to a "weak-amplitude-object"; it is then somewhat difficult to obtain QP information from the object, such as thickness and refractive index data. In addition to microscopic imaging methods, various optical interferometers have also been developed to obtain QP images. One specific example is the phase-shift interferometer that was proposed by Bruning et al.,[3] where a piezoelectric device-driven stage and an imaging camera were combined with a Twyman–Green interferometer. While the phase resolution of the resulting interferometer exceeded $\lambda/100$, the hysteresis of the piezo-actuator and the resulting phase noise reduced its overall stability. To solve the stability problem and further enhance the measurement accuracy, Kadono et al. used a common-path polarized-light interferometer for phase shift imaging.[4] Subsequently, the highly important Hilbert phase microscope was developed by Ikeda et al. for observation of dynamic phenomena using single-shot measurements.[5] Among the various phase imaging microscopes that have been proposed, the diffraction phase microscope (DPM)[6] proposed by Popescu et al. seems most promising for many practical applications in light of its real-time measurement capabilities and its stability.[7,8] The DPM uses a common-path interferometric method and can be built easily for use as a QPI module for attachment to a commercially-available optical microscope.

In construction of the DPM, the speckle noise that is introduced when a high-coherence laser is used as a light source often causes system performance degradation. Therefore, a temporally low-coherence light source is generally used,[8–10] and this results in low spatial coherence on the sample plane. However, an illumination light source with high spatial coherence is required to reconstruct the QP image with high accuracy.[11,12] These two contradicting requirements lead to the use of a relatively broad-band light source with a low-numerical-aperture (NA) condenser lens in these microscopes. In addition, for common-path interferometric measurements, a small-diameter pinhole is required to perform spatial filtering. Therefore, DPM inevitably forces us to measure low-light-intensity images, which results in requirements for a high-intensity light source and/or a very-high-sensitivity (cooled) image detector.

To overcome these problems, we introduce a technique known as a single-pixel imaging (SPI).[13,14] SPI is a scanning-free multiplex imaging method in which a series of spatially-coded masks and a single-channel detector are used. The use of the single-channel detector means that a high-sensitivity detector such as a photomultiplier tube (PMT) can also be used.[15–17] Through introduction of a time-resolved technique, high-speed repetitive phenomena can also be observed if desired. Simultaneous multispectral imaging may also become more easily possible by introduction of a multi-frequency lock-in detection scheme, as will be discussed later in the paper. Furthermore, the advantages of multiplexing in the spatial domain may also be retained.[18,19] If necessary, a compressive sensing (CS) technique can be introduced to reduce the measurement time.[20] Numerous reports on SPI can therefore be found in the literature, including three-dimensional imaging,[21] terahertz-frequency region imaging,[22] high spatial-resolution imaging,[23] profilometry,[24] and optical comb spectro-imaging[25] techniques. Recently, a combination of a phase imaging method with SPI was reported.[18,25,26]

In this paper, we propose DPM combined with SPI (SPI-DPM), which has some advantages mentioned above. However, one of the drawbacks of SPI is that the dynamic range of the detection system is insufficient: the ordinate resolution

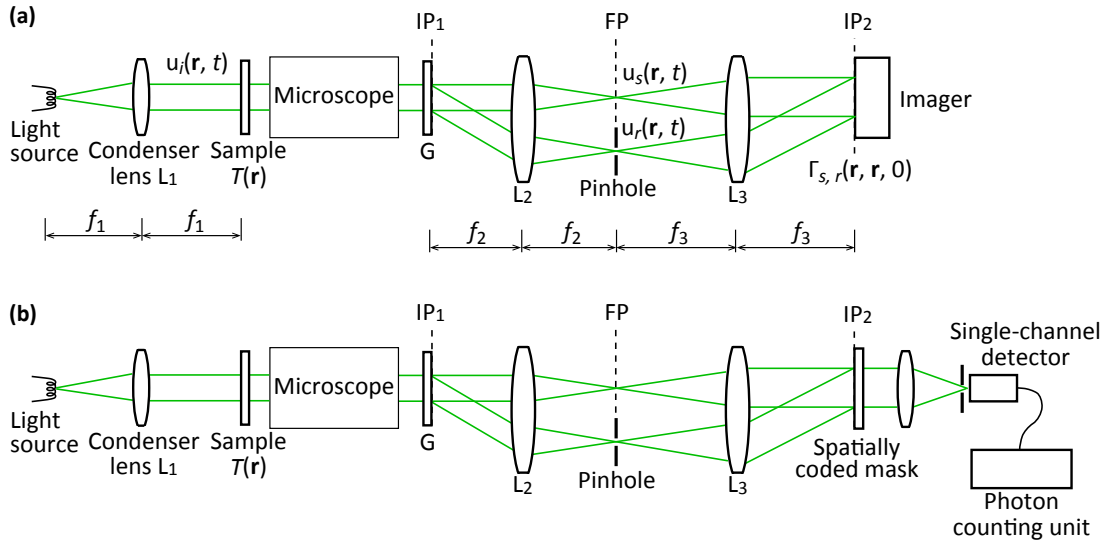

Fig. 1. (Color online) Schematic of a common-path interferometric DPM; (a) conventional DPM, and (b) PC-SPI-DPM. $u_i(\mathbf{r}, t)$ is the illumination field, and $u_s(\mathbf{r}, t)$ and $u_r(\mathbf{r}, t)$ are the sample and reference field, respectively. $\Gamma_{s,r}(\mathbf{r}, \mathbf{r}, 0)$ is the spatially-dependent, temporal cross-correlation function evaluated at a time delay zero ($\tau = 0$) on the imager (see Appendix).

of the analog-to-digital converter (ADC) that is connected after the PMT is not generally enough. For accurate reconstruction of the image of a sample object with a complex spatial structure, the ordinate resolution of the ADC must be increased as far as possible. Another problem with SPI is that it is a difficult technique to perform under the low-light-intensity conditions of DPM. Therefore, the overall performance of SPI-DPM often results in being almost the same as that of the conventional DPM, depending on the measurement conditions and/or the instrumental setups. In the present paper, therefore, we further propose the introduction of a photon-counting (PC) technique to produce PC-based SPI-DPM (PC-SPI-DPM). PC is carried out with ease following the introduction of the PMT to SPI. We describe the instrumentation setup in detail along with its basic performance. As a proof-of-principle experiment, we measured the thickness of a transparent indium tin oxide (ITO) layer coated on a silica glass substrate, where a brief comparison of the performance is made between the SPI-DPM and the PC-SPI-DPM scheme for demonstrating the superiority of the latter to the former. We discuss the basic performance of PC-SPI-DPM and future modifications to the system.

2. DPM and PC-SPI-DPM

In this section, we explain the conventional common-path DPM and our PC-SPI-DPM briefly. Figure 1(a) shows a schematic of the conventional DPM proposed by Popescu et al.[6] In DPM, unlike the "traditional" interferometric method, in which the reference $u_r(\mathbf{r}, t)$ and the sample field $u_s(\mathbf{r}, t)$ are generated separately from the illumination field $u_i(\mathbf{r}, t)$, the reference field is generated from the sample field by using a plane diffraction grating G that is placed on the image plane IP_1 of the microscope. The reference field is derived from the diffracted first-order light by passing through a spatial filter (pinhole) put on the Fourier plane (FP) of a lens L_2. The reference field, together with the zeroth-order diffracted light, i.e., the sample field, after passing through a Fourier transform lens L_3, makes an interference fringe pattern on the detector plane IP_2. From the interference pattern, the phase image of the sample is derived. The theoretical aspect of the common-path DPM in phase measurement is summarized in Appendix. For successful measurement of the phase image, the numerical aperture (NA) of the condenser lens L_1 should be small as possible to guarantee the spatial coherence on the sample plane. In addition, the diameter of the pinhole should be small as possible. Therefore, although the DPM has a powerful advantage in robustness against the external vibration noise, its optical throughput is not quite high.

In order to relax the optical throughput problem in the DPM, we introduce the PC-SPI technique in the present paper, whose scheme is shown in Fig. 1(b). On the detector plane, we put a spatially coded mask, by which the interference pattern is spatially coded by a series of Hadamard matrix-based masks. The coded light flux is detected by a single-channel detector as a time-series data. Then, the interference pattern is reconstructed by the inverse-Hadamard transform, from which the phase image is derived. In the PC-SPI-DPM, the optical throughput problem is overcome to some extent, because we can employ a high-sensitive single-channel detector such as a photomultiplier tube (PMT) and might be able to expect the spatial multiplex advantage in light detection. In addition, the PC technique enhances the sensitivity in weak light measurements, which also overcomes the dynamic range problem that is inherent to SPI.

3. Experimental methods

Figure 2 shows a schematic of the actual PC-SPI-DPM setup, which consists of four parts: a light source, a transmission microscope, an additional DPM module, and an SPI system. The red dotted lines and green solid lines show the typical imaging and illumination rays, respectively. A commercially available transmission inverted-type microscope (Nikon ECLIPSE Ts2) was used and we replaced its light source with a high-brightness surface-emitting LED (Luminus Devices PT-121-TE, center emission wavelength: 528 nm) that is driven by a 10 A direct current. It was important to use a light source here that combined high spatial coherence with such high intensity for DPM to be performed successfully.

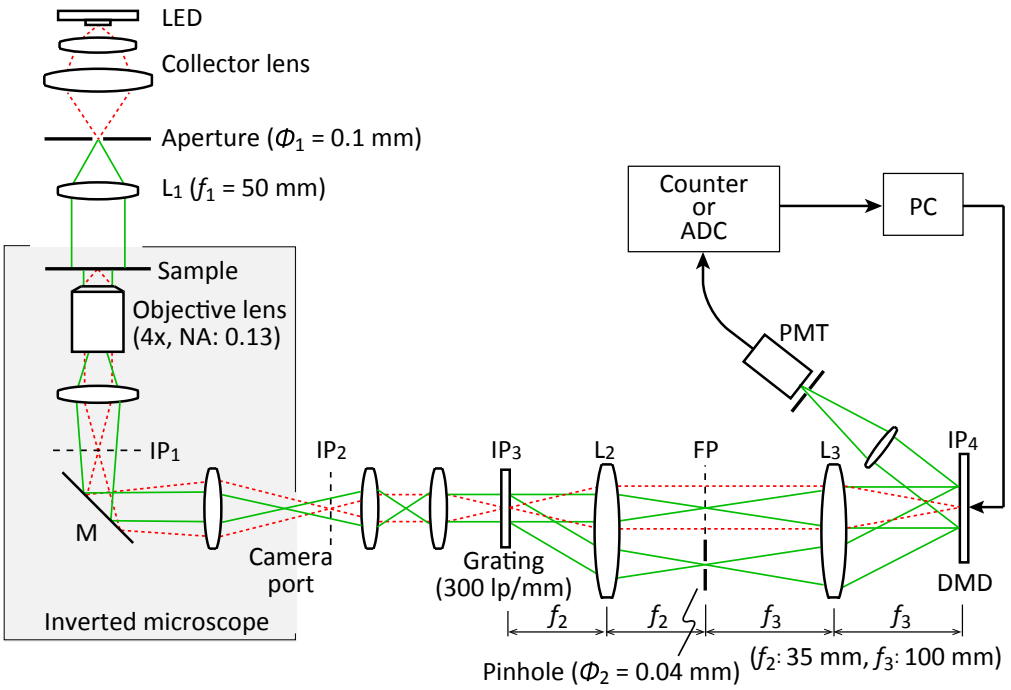

Fig. 2. (Color online) Schematic of the PC-SPI-DPM system. LED: light-emitting diode; IP_1–IP_4: image planes; L_1–L_3: lenses; FP: Fourier plane; DMD: digital mirror device; PMT: photomultiplier tube; ADC: analog-to-digital converter. Red dotted lines indicate the imaging rays and green solid lines indicate the illumination rays.

Therefore, we placed an aperture (diameter: $\phi_1 = 100\,\mu m$) on the light source image plane and then illuminated the sample object using an $f_1 = 50\,mm$ collimator lens L_1. The NA of the illumination system, which is given by ϕ_1/f_1, was thus approximately 0.002, which was extremely small but guaranteed the spatial coherence on the sample plane, as was already mentioned.[11,12)]

As a test sample, we used a ~100-nm-thick transparent ITO layer that was coated on a silica glass substrate (EHC SZ-B111P6N). The image of the sample was focused on a plane denoted by IP_1 using an objective lens (4×, with NA of 0.13) and was then relayed to the subsequent conjugate planes, IP_2–IP_4, in the DPM module. The IP_2 plane is an output camera port of the microscope. A transmission-type blazed grating (G; Edmund Optics #49-575, 300 grooves/mm; blaze angle of 17.5° at 520 nm) was placed on the IP_3 plane. For the purposes of common-path interferometric measurements, we placed a pinhole (diameter $\phi_2 = 40\,\mu m$) on a FP at the middle of a $2f_2$–$2f_3$ optics configuration (where $f_2 = 35\,mm$ and $f_3 = 100\,mm$). The role of the pinhole was to spatially filter the first-order diffracted light at the FP (~5 nm spectral bandwidth), while the zeroth-order light passed through unchanged. The zeroth- and the first-order light beams then interfere with each other to generate a sinusoidal fringe pattern (i.e., an interferogram) on the final IP_4 plane. In a conventional DPM, an imaging camera is located on this IP_4 plane to capture the interferogram. However, we inserted a digital mirror device (DMD; Texas Instruments DLP LightCrafter Display 2010) for SPI, which allowed the interferogram images to be spatially coded sequentially.

We used a 128 × 128 pixel-sized coding mask that corresponded to 384 × 384 micro-mirrors in the DMD. Because the micro-mirror pitch was 5.4 μm, the mask pitch became 16.2 μm and the region of interest (ROI) on the DMD was then $2.07 \times 2.07\,mm^2$. The period p of the fringe pattern that was introduced as a spatial frequency carrier is given by $\sim M\Lambda = 9.5\,\mu m$,[27)] where M is the magnification factor of the $2f_2$–$2f_3$ optics configuration and Λ is the grating period. This value of p was too small to satisfy the Nyquist sampling criterion for the mask pitch. Therefore, we added a 15× magnifying lens (not shown in the figure) to the setup, which resulted in an actual magnification factor of 42.9. As a result, the period of the fringe pattern on the DMD was 142.5 μm, which corresponded to ~26 micro-mirrors on the DMD and ~14 fringes in the ROI. Other important factors in DPM design are the aperture diameter ϕ_1 and the pinhole diameter ϕ_2. In our setting, $\phi_1/f_1 = 0.002$ was determined based on the work of Refs. 11 and 12. The value of $\phi_2 = 40\,\mu m$ was determined by taking a trade-off between the light intensity and the phase ambiguity into account.

We used the Hadamard transform imaging (HTI) method,[13)] in which a series of orthogonal coded masks based on a Hadamard matrix were used. The light flux that was reflected by the DMD was fed into the PMT (Hamamatsu Photonics H6780-01) and then recorded as time-series data. The PC technique was then used here to gather the low-intensity light flux and enlarge the dynamic range of the detection system. The photoelectron pulses that were obtained from the PMT were pulse-amplified (Hamamatsu Photonics C6438-01) and discriminated and were then fed into a laboratory-made counter unit that collected the pulses that arrived within a predetermined time interval after each mask exchange.

Finally, the interferogram image was reconstructed using the inverse Hadamard transform. Two methods can be used to retrieve the QP image from the reconstructed interferogram: a Fourier transform method[28)] and a Hilbert transform method.[5)] Although the two methods are essentially the same in light of the frequency filtering, we used the Fourier transform method because it does not require an additional null measurement to eliminate the carrier frequency component.

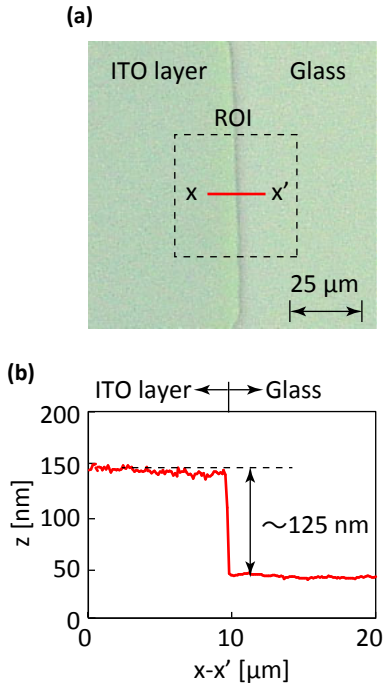

Fig. 3. (Color online) (a) Transmission image of the sample. The region of interest (ROI) is indicated by the dashed square ($48.3 \times 48.3\,\mu m^2$). (b) Cross-section profile of the line x–x' shown in (a) that was measured using the AFM. The thickness of the ITO layer on the silica-glass substrate is ~125 nm.

4. Results

4.1 Thickness measurement of the transparent thin layer

As a proof-of-principle experiment, we measured the thickness of a transparent ITO layer that was coated on a silica-glass substrate. Figure 3(a) shows a transmission image of the sample in which the ROI is indicated by a dashed square ($48.3 \times 48.3\,\mu m^2$). A step in thickness from the ITO layer to the silica-glass substrate exists along the red line x–x'. Figure 3(b) shows the cross-section profile that was measured using an atomic force microscope (Olympus OLS3500-PTU, depth resolution: 1.0 nm). The step height was approximately 125 nm.

As mentioned in the previous section, the dynamic range of the signal detection system affects the reconstructed image accuracy greatly in SPI. This is because the entirety of the spatial information of the coded object is summed in the single-channel detector. It is therefore important to discriminate any slight differences in the detected signals. The PC-SPI scheme proposed here offers an appropriate solution because PC in principle has no limit on its dynamic range as the measurement time increases. To verify the effectiveness of PC-SPI-DPM, we compared QP images that were obtained from an analog-based SPI-DPM and the proposed PC-SPI-DPM. The number of illumination masks used was $N = 16{,}384$ for the 128×128 pixel size.

Figure 4(a) shows a interferogram image that was reconstructed using the analog-based SPI, where we used a 12-bit ADC, and the time constant of the low-pass filter that was connected after the PMT was 40 ms (load resistance: 1 MΩ; capacitance: 0.01 μF). Figure 4(b) shows the power spectrum image of the interferogram image shown in (a), while its cross-sectional profile along the line A–A′ is shown in a lower figure, in which we can see a high DC background and two small interference peaks. By applying the Fourier transform method[28] to the interferogram image, we then obtained the QP image shown in Fig. 4(c). However, this phase image does not represent the original object correctly; the cross-sectional profile along the line B–B′ differs from that of the original that was shown in Fig. 3(b). This occurs because a low signal-to-noise ratio (SNR) was obtained for the reconstructed interferogram image because of the limited dynamic range of the ADC.

Figure 4(d) shows an interferogram that was obtained from PC-SPI where the number of photons counted was $\sim 4 \times 10^5$ counts/pattern. The measurement time was the same as that used for the analog-based method: 40 ms/pattern. The power spectrum image shown in Fig. 4(e) and the resulting QP image that is shown in Fig. 4(f) are both clearer than that obtained from the analogue-based method; we were then able to obtain the QP image of the ITO layer correctly. This occurred because of the dynamic range expansion of the detection system from 4,096 (12 bits) to $\sim 4 \times 10^5$. To obtain further clear image, we increased the number of photons to $\sim 4 \times 10^6$ count/pattern by increasing the measurement time: 400 ms/pattern. The results are shown in Figs. 4(g)–4(i). We were then able to obtain an interferogram image with high visibility and a power spectrum with a high SNR. The QP image that was finally obtained was much closer to the original one. Taking the refractive index of the ITO layer, which is 1.89 at a wavelength of 550 nm,[29] into account, the phase step of 1.32 radians along the line B–B′ that is shown in Fig. 4(i) corresponds to the optical thickness of the layer at approximately 125 nm, which agreed well with the corresponding thickness that was measured using AFM.

4.2 Evaluation of the image quality

To evaluate the PC-SPI-DPM system's performance, we calculated the SNR of the reconstructed interferogram image as a function of the average number of photons that arrived during a single period of illumination (exposure) of the mask pattern. We defined the SNR here as the ratio of the peak value of the first-order interference component to the averaged noise floor, as shown in Fig. 5(a). The sample object was the same as that which was used in Fig. 4. Figure 5(b) shows the calculated result, where the dotted line represents a logarithmic fit to the plot. This result indicates that the SNR in the PC-SPI-DPM increased with increasing numbers of photons, as expected. Next, we evaluated the phase noise in the reconstructed QP image. The ROIs that were used for this evaluation are shown in Fig. 5(c), where the regions of phase images P_1 and P_2 represent the ITO layer and the silica glass, respectively. We defined the phase error as a spatial standard deviation (SD) for both the P_1 and P_2 regions. Figure 5(d) shows a plot of the SD versus the average number of photons arriving during the single period of illumination of the mask pattern. The phase noise in the QP image decreased with increasing numbers of photons. These results indicate that the proposed PC-SPI-DPM system works reasonably well.

5. Discussion and Conclusions

In microscopic QPI, DPM appears promising from the perspective of its robustness, with equipment that can easily be constructed as a module for attachment to a commercially-

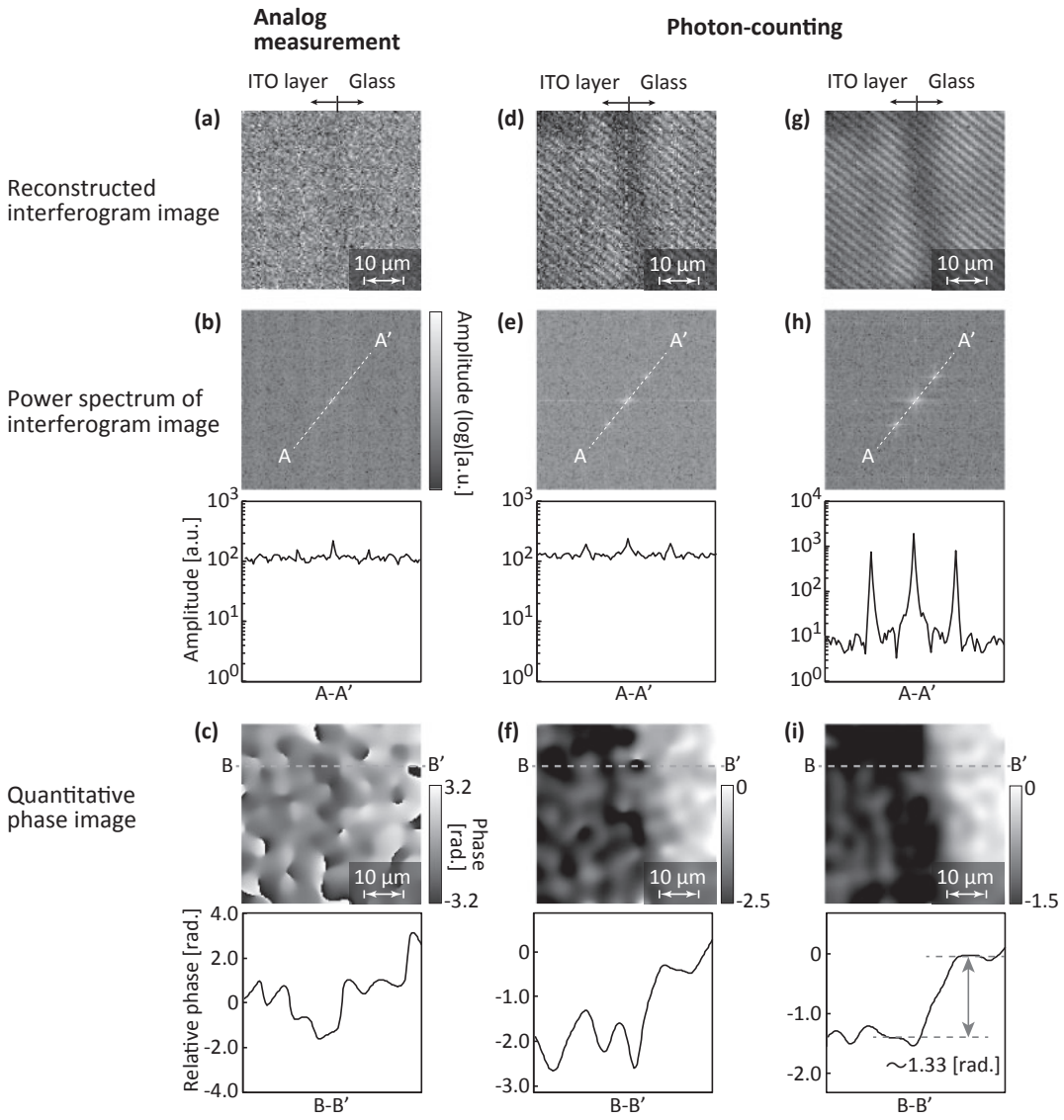

Fig. 4. Measurement results for the thickness of the ITO layer when coated on a silica glass substrate by SPI-DPM. The left column (a)–(c) shows the results that were obtained from analogue-based SPI-DPM (40 ms/pattern), while the center column (d)–(f) shows the results that were obtained from the PC-SPI-DPM ($\sim 4 \times 10^5$ counts, 40 ms/pattern), and the right column (g)–(i) shows the results obtained from PC-SPI-DPM ($\sim 4 \times 10^6$ counts, 400 ms/pattern). The upper row shows the reconstructed interferogram images, while the center row shows power spectrum images and profiles along the A–A′ lines, and the lower row shows QP images and cross-sectional profiles along the B–B′ lines.

available microscope. However, the optical throughput of DPM is generally low because it requires high spatial coherence for the light used to illuminate the sample and also requires use of a pinhole for spatial filtering. In our optical setup, the light power was reduced by ~1/2,000 over the path from the object plane to interference plane IP_4. Therefore, a high-intensity light source and a high-sensitivity image detector were both required. We therefore used a high-brightness LED as the light source and also introduced the SPI technique, which allowed us to use a high-sensitivity PMT. Use of the PMT brought another bonus: the introduction of the PC technique, by which the sensitivity problem in DPM and the dynamic range problem in SPI were both solved simultaneously. One unsolved problem that remains in PC-SPI-DPM is the measurement time. For example, it took approximately 10 min to obtain the phase image that is shown in Fig. 4(f). We therefore aim to design a more compact optical system that has higher optical throughput and/or attempt to enhance the light gathering efficiency during the treatment of the DMD.[30–33] If necessary, we may use the CS technique to reduce the measurement time.

Three methods have been proposed to obtain multi-colored (spectroscopic) QP images to date: one involves the use of a combination of a white light source and a spectroscopic filter,[9] the second uses multiple monochromatic light sources and a RGB camera to give separate red, green, and blue images,[34] and the third uses a spatial filter that transmits the first- and second-order diffracted light beams simultaneously.[27] However, the proposed SPI-DPM scheme offers another possibility to obtain these multi-colored phase images more precisely. One example is shown in Fig. 6(a). In this setup, an inlet for an optical fiber for a multichannel spectrometer is placed at the location of the PMT that was shown in Fig. 2. If a spectral scan is carried out for each mask pattern exchange of the DMD, the QP image could then be reconstructed for each wavelength element in the same manner as that shown in Fig. 2. This scheme may be useful in obtaining the dispersion relation of the sample. Figure 6(b)

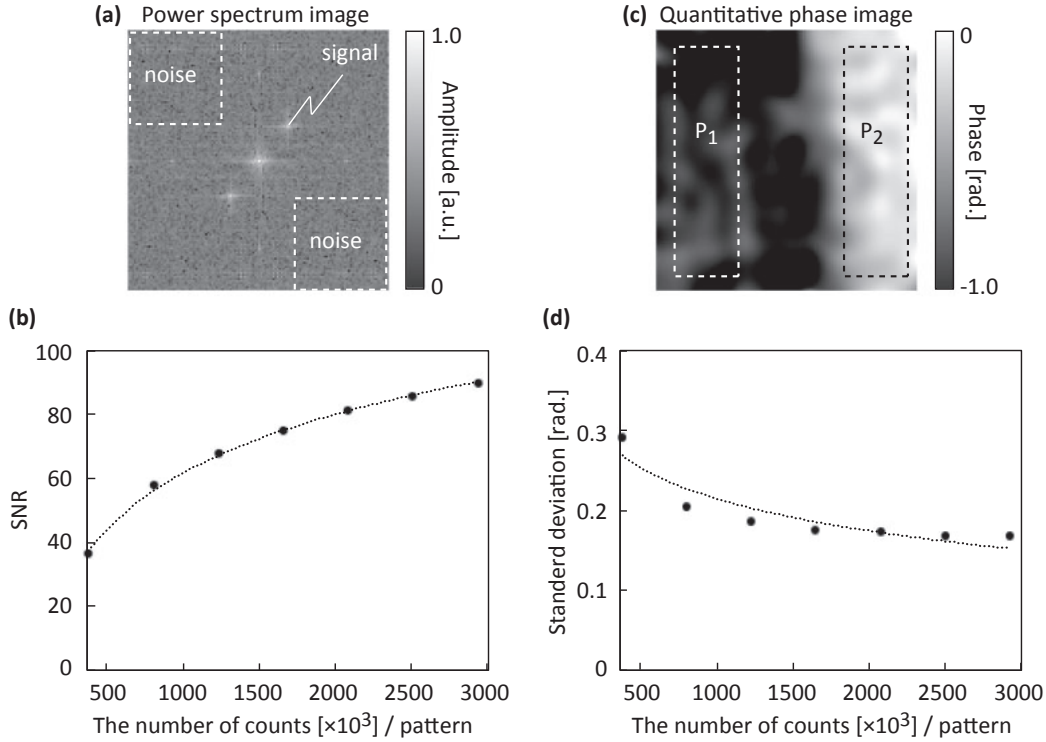

Fig. 5. Evaluation of the quality of the images that can be obtained using the PC-SPI-DPM system. (a) Typical power spectrum image, where the sample object was the same as that which was measured in Fig. 4. (b) Plot of SNR versus the number of photons arriving during a single period of illumination of the mask pattern, where the dotted line indicates a logarithmic fit to the plot. (c) A typical reconstructed QP image, where the areas of P_1 and P_2 represent the ITO layer and the silica glass, respectively. (d) Plot of the SD versus the average number of photons arriving during a single period of illumination of the mask pattern.

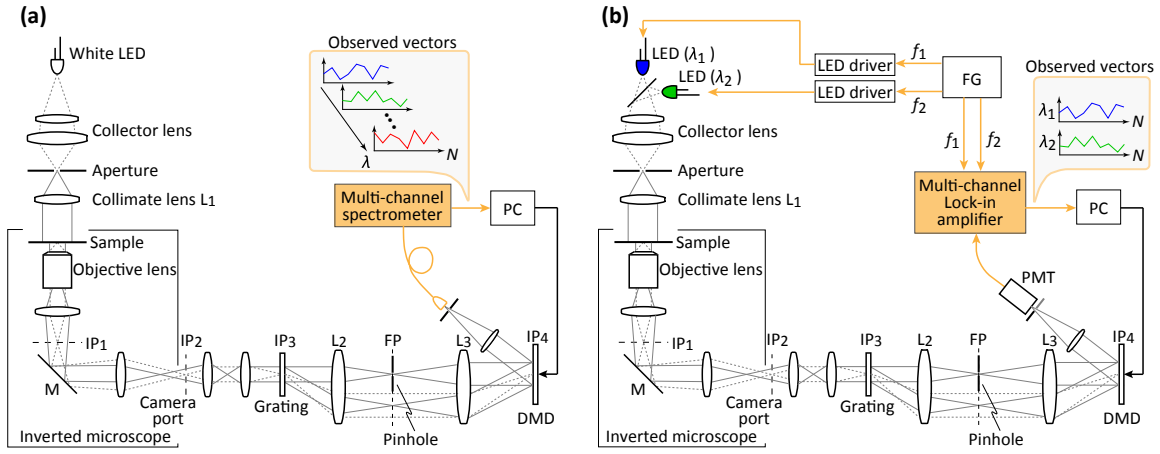

Fig. 6. (Color online) Possible future extensions of the SPI-DPM scheme. (a) A multi-spectral QPI system and (b) a multi-color multichannel-lock-in QPI system.

shows another possible example: a multichannel lock-in QPI system. In this case, we use plural LEDs that are modulated at different frequencies as the light sources. The output signal from the PMT is fed into a multichannel lock-in amplifier, from which we could then obtain the multi-colored QP images simultaneously. A PC-based digital lock-in amplifier would be used for the low-intensity light. Another scheme that could be realized by the introduction of SPI is time-resolved QPI for a repeatable phenomenon, which can be conducted in the manner shown in Refs. 16 and 25.

Appendix: Theoretical aspect of DPM in phase measurement

In this Appendix, a brief review on the theoretical aspect of the common-path DPM in phase measurement is given according to the Popescu and his coworkers' paper.[11,12] In the "traditional" interferometry, when the illumination field is expressed by $u_i(\mathbf{r}, t)$ as a function of the two-dimensional position vector $\mathbf{r}$ and time t, the reference field $u_r(\mathbf{r}, t)$ and the sample field $u_s(\mathbf{r}, t)$ are given by $u_i(\mathbf{r}, t)$ and $T(\mathbf{r})u_i(\mathbf{r}, t)$, respectively, where $T(\mathbf{r})$ is the transmittance of the sample. Then, the spatially-dependent, temporal cross-correlation function at a time delay zero ($\tau = 0$) is given by $\Gamma_{s,r}(\mathbf{r}, \mathbf{r}, 0) = \langle u_s(\mathbf{r}, t) u_r^*(\mathbf{r}, t) \rangle$, where the symbol $\langle \cdots \rangle$ stands for the ensemble average and * does complex conjugate. From the generalized Wiener–Khintchine theorem, $\Gamma_{s,r}(\mathbf{r}, \mathbf{r}, 0) = \int W_{s,r}(\mathbf{r}, \mathbf{r}, \omega)\, d\omega$ with $W_{s,r}(\mathbf{r}, \mathbf{r}, \omega) = \langle U_s(\mathbf{r}, \omega) U_r^*(\mathbf{r}, \omega) \rangle$, where $W_{s,r}(\mathbf{r}, \mathbf{r}, \omega)$ is the cross-spectral density and $U_s(\mathbf{r}, \omega)$

and $U_r(\mathbf{r},\omega)$ are Fourier transforms of $u_s(\mathbf{r},t)$ and $u_r(\mathbf{r},t)$, respectively. Then, $\Gamma_{s,r}(\mathbf{r},\mathbf{r},0) = T(\mathbf{r})\langle U_i(\mathbf{r},\omega)U_i^*(\mathbf{r},\omega)\rangle$ and, therefore, $\arg[\Gamma_{s,r}(\mathbf{r},\mathbf{r},0)] = \arg[T(\mathbf{r})]$: we can obtain the true phase image.

In the case of the common-path QPM, the reference field $U_r(\mathbf{r},\omega)$ is derived from the sample field $U_s(\mathbf{r},\omega)$: $U_r(\mathbf{r},\omega) = \int U_s(\mathbf{r}',\omega)h_0(\mathbf{r}-\mathbf{r}')\,d\mathbf{r}'$, where $h_0(\mathbf{r})$ is the Fourier transform of the geometric shape of the spatial filter inserted in the Fourier plane of the lens L_2 as shown in Fig. 1(a). Therefore, when the spatial filter is a pinhole with a very small diameter (expressed by a delta function), $h_0(\mathbf{r})$ becomes a constant value allover at the detector plane IP_2. On the contrary, without the spatial filter, $h_0(\mathbf{r})$ approaches a delta function. Then, $\Gamma_{s,r}(\mathbf{r},\mathbf{r},0)$ at the detector plane is given by

$$\Gamma_{s,r}(\mathbf{r},\mathbf{r},0) = \int W_{s,r}(\mathbf{r},\mathbf{r},0)\,d\omega = \int \langle U_s(\mathbf{r},\omega)U_r^*(\mathbf{r},\omega)\rangle\,d\omega = T(\mathbf{r})\iint W_i(\mathbf{r},\mathbf{r}',\omega)\,d\omega\,h_0^*(\mathbf{r}-\mathbf{r}')T^*(\mathbf{r}')\,d\mathbf{r}', \tag{A·1}$$

where $W_i(\mathbf{r},\mathbf{r}',\omega) = \langle U_i(\mathbf{r},\omega)U_i^*(\mathbf{r}',\omega)\rangle$ is the cross-spectral density of the illumination field on the sample plane. Here we assumed that the sample plane and the detector plane were expressed by the same position vector $\mathbf{r}$ for simplicity. Because the fields are usually statistically stationary, $W_i(\mathbf{r},\mathbf{r}',\omega)$ can be expressed as $W_i(\mathbf{r}-\mathbf{r}',\omega)$. Hence,

$$\Gamma_{s,r}(\mathbf{r},\mathbf{r},0) = T(\mathbf{r})\iint W_i(\mathbf{r}-\mathbf{r},\omega)\,d\omega\,h_0^*(\mathbf{r}-\mathbf{r}')T^*(\mathbf{r}')\,d\mathbf{r}' = T(\mathbf{r})\left(\int T(\mathbf{r}')\Gamma_i^*(\mathbf{r}-\mathbf{r}')h_0(\mathbf{r}-\mathbf{r}')\,d\mathbf{r}'\right)^*. \tag{A·2}$$

The quantitative phase finally obtainable is therefore given by

$$\arg[\Gamma_{s,r}(\mathbf{r},\mathbf{r},0)] = \arg[T(\mathbf{r})] - \arg\left[\int T(\mathbf{r}')\Gamma_i^*(\mathbf{r}-\mathbf{r}')h_0(\mathbf{r}-\mathbf{r}')\,d\mathbf{r}'\right]. \tag{A·3}$$

If the NA of the illumination condenser lens L_1 approaches zero, $\Gamma_i(\mathbf{r}-\mathbf{r}')$ will be a constant value, resulting in the spatially-coherent illumination. If the NA becomes large, it will be a delta function, resulting in the spatially-incoherent illumination. From Eq. (A·3), we can find that the complete phase image, $\arg[T(\mathbf{r})]$, is obtainable at the cost of the optical throughput, only when both of $\Gamma_i(\mathbf{r})$ and $h_0(\mathbf{r})$ are constant values, i.e., only when the spatially-coherent illumination and the delta-function-like spatial filtering. Otherwise, $\arg[\Gamma_{s,r}(\mathbf{r},\mathbf{r},0)]$ cannot be equal to $\arg[T(\mathbf{r})]$: the high spatial-frequency component of the phase image of the sample is lost. This is the essential point in designing the DPM system. The aim of the present paper is to relax the optical throughput problem by introducing the PC-based SPI technique to the DPM as mentioned in the text and shown in Fig. 1(b).

Acknowledgments

This work was supported by a Grant-in-Aid for JSPS Research Fellows (No. 16J08197) from the Ministry of Education, Culture, Sports, Science, and Technology of Japan. The authors thank Dr. T. Okamoto and Mr. S. Kamada of Tokushima University for their help with the AFM measurements.

1) F. Zernike, Physica **9**, 686 (1942).
2) F. H. Smith, Research (London) **8**, 385 (1955).
3) J. H. Bruning, D. R. Herriott, J. E. Gallagher, D. P. Rosenfeld, A. D. White, and D. J. Brangaccio, Appl. Opt. **13**, 2693 (1974).
4) H. Kadono, N. Takai, and T. Asakura, Appl. Opt. **26**, 898 (1987).
5) T. Ikeda, G. Popescu, R. R. Dasari, and M. S. Feld, Opt. Lett. **30**, 1165 (2005).
6) G. Popescu, T. Ikeda, R. R. Dasari, and M. S. Feld, Opt. Lett. **31**, 775 (2006).
7) J. Jung, K. Kim, J. Yoon, and Y. Park, Opt. Express **24**, 2006 (2016).
8) C. E. Cordeiro, O. Abilez, T. Gupta, G. Goetz, O. Solgaard, and D. Palanker, CLEO, 2017, AW4A.5.
9) Y. Park, T. Yamauchi, W. Choi, R. Dasari, and M. S. Feld, Opt. Lett. **34**, 3668 (2009).
10) B. Bhaduri, H. Pham, M. Mir, and G. Popescu, Opt. Lett. **37**, 1094 (2012).
11) T. H. Nguyen, C. Edwards, L. L. Goddard, and G. Popescu, Opt. Lett. **39**, 5511 (2014).
12) C. Edwards, B. Bhaduri, T. Nguyen, B. G. Griffin, H. Pham, T. Kim, G. Popescu, and L. L. Goddard, Opt. Express **22**, 5133 (2014).
13) W. K. Pratt, J. Kane, and H. C. Andrews, Proc. IEEE **57**, 58 (1969).
14) J. H. Shapiro, Phys. Rev. A **78**, 061802 (2008).
15) V. Studer, J. Bobin, M. Chahid, H. S. Mousavi, E. Candes, and M. Dahan, Proc. Natl. Acad. Sci. U.S.A. **109**, E1679 (2012).
16) T. Mizuno and T. Iwata, Opt. Express **24**, 8202 (2016).
17) B. Lochocki, A. Gambín, S. Manzanera, E. Irles, E. Tajahuerce, J. Lancis, and P. Artal, Optica **3**, 1056 (2016).
18) P. Clemente, V. Durán, E. Tajahuerce, P. Andrés, V. Climent, and J. Lancis, Opt. Lett. **38**, 2524 (2013).
19) K. Shibuya, K. Nakae, Y. Mizutani, and T. Iwata, Opt. Rev. **22**, 897 (2015).
20) M. F. Duarte, M. A. Davenport, D. Takbar, J. N. Laska, T. Sun, K. F. Kelly, and R. G. Baraniuk, IEEE Signal Process. Mag. **25**, 83 (2008).
21) B. Sun, M. P. Edgar, R. Bowman, L. E. Vittert, S. Welsh, A. Bowman, and M. J. Padgett, Science **340**, 844 (2013).
22) D. Shrekenhamer, C. M. Watts, and W. J. Padilla, Opt. Express **21**, 12507 (2013).
23) S. Tetsuno, K. Shibuya, and T. Iwata, Opt. Express **25**, 3420 (2017).
24) Q. D. Pham and Y. Hayasaki, Appl. Opt. **54**, A39 (2015).
25) K. Shibuya, T. Minamikawa, Y. Mizutani, H. Yamamoto, K. Minoshima, T. Yasui, and T. Iwata, Opt. Express **25**, 21947 (2017).
26) P. A. Stockton, J. J. Field, and R. A. Bartels, Methods (in press) [DOI: 10.1016/j.ymeth.2017.10.007].
27) M. R. Jafarfard, S. Moon, B. Tayebi, and D. Y. Kim, Opt. Lett. **39**, 2908 (2014).
28) M. Takeda, H. Ina, and S. Kobayashi, J. Opt. Soc. Am. **72**, 156 (1982).
29) J. A. Woollam, W. A. McGaham, and B. Johs, Thin Solid Films **241**, 44 (1994).
30) L. Streeter, G. R. Burling-Claridge, M. J. Cree, and R. Künnemeyer, Appl. Opt. **48**, 2078 (2009).
31) W.-K. Yu, X.-F. Liu, X.-R. Yao, C. Wang, Y. Zhai, and G.-J. Zhai, Sci. Rep. **4**, 5834 (2014).
32) F. Soldevila, P. Clemente, E. Tajahuerce, N. Uribe-Patarroyo, P. Andrés, and J. Lancis, Sci. Rep. **6**, 29181 (2016).
33) B. Lochocki, A. Gambín-Regadera, and P. Artal, Appl. Opt. **55**, 10198 (2016).
34) Y. Jang, J. Jang, and Y. Park, Opt. Express **20**, 9673 (2012).